LIF measurements on an atomic helium beam in the edge of a fusion plasma

M Krychowiak[1)], Ph Mertens[2)], R König[1)], B Schweer[2)], S Brezinsek[2)], O Schmitz[2)], M Brix[3)], U Samm[2)], T Klinger[1)]
[1)]*Max-Planck-Institut für Plasmaphysik, EURATOM-Association, Greifswald, Germany*
[2)]*Institut für Energieforschung (Plasmaphysik), FZ Jülich, EURATOM-Association, TEC, Jülich, Germany and*
[3)]*UKEA, JET- Experimental Department, EURATOM-Association,*
Culham Science Centre, ABINGDON, Oxfordshire, OX14 3DB, U.K.[*]

A method for absolute measurement of population densities of selected atomic helium levels, which has been applied on the tokamak TEXTOR at the Forschungszentrum Jülich in Germany, is presented. The method is based on the resonant excitation of selected levels by a high-power, narrow-band, pulsed laser beam saturating the optical pumping process. Observation of the fluorescence response is performed at the laser wavelength and elsewhere in the spectrum: this gives information on collisional population transfer between some excited levels. Data analysis, as required for the derivation of absolute population densities, includes due consideration of the Zeeman splitting of spectral lines in a strong magnetic field. First results of the measured population densities are compared with those provided by simulation based on the collisional-radiative model for atomic helium in the edge of fusion plasmas. This code has been extended to include the laser interaction with atomic helium, in order to simulate the measured time traces of radiation from the laser-perturbed levels. Combination of this simulation procedure with laser-induced fluorescence measurements is suggested as a possible method for determining the electron density in the edge plasma.

I. INTRODUCTION

Line radiation of atomic helium is used for determination of spatially and temporally resolved electron density and temperature in the plasma. In the edge region of fusion plasmas helium is introduced radially into the plasma in form of thermal [1] or supersonic beams [2–5]. The method is based on intensity measurement of three spectral lines of atomic helium. Electron density and temperature are obtained by comparing two line intensity ratios, with main dependence on either n_e or T_e, with those calculated using a collisional-radiative (CR) model for helium. Hence, the accuracy of the n_e and T_e derivation depends on the reliability of the model which contains among other a large number of rate coefficients for electron collisional excitation and ionisation [2, 6–11]. Most of these parameters – at least for higher temperatures as diagnosed with helium beams in fusion edge plasmas – are known only from calculations. Comparison of measured passive helium line radiation of a supersonic helium beam installed on TEXTOR with CR modelling results by Brix showed some deviations between calculated and measured line intensities as well as penetration depth of the beam into the plasma [2] making clear that the helium modelling in the fusion edge plasma needs a further improvement. The laser-induced fluorescence (LIF) spectroscopy applied on a thermal helium beam on TEXTOR, described in this paper, was used in order to validate some parameters of the CR model and its prediction on the population of selected levels of the beam atoms.

LIF is a widely used method to obtain several kinds of local information about a plasma [12, 13]: particle behaviour (velocity distribution by the Doppler effect [14, 15], diffusion coefficient [16]), the electric and magnetic fields (Stark [17] and Zeeman effect [18]). By the feasibility of particle density measurement in a selected quantum level and by analysing of collision-induced fluorescence signals, also investigations of collisional-radiative models are possible using LIF [19, 20]. In this work, we used LIF spectroscopy to validate the model prediction of some level populations of atomic helium. The metastable levels ($2^{1,3}$S) as well as the $2^{1,3}$P$^\mathrm{o}$ states are in principle accessible by this method, complementing earlier passive visible spectroscopic investigations [2, 8, 10, 21–23]. Moreover, the rate coefficients for collisional transfer between excited levels (e.g. between levels with $n = 3$) can be derived from collision-induced fluorescence signals. Sensitivity analyses show that these coefficients may play an important role in the improvement of the model for helium [24].

On the tokamak TEXTOR at the Forschungszentrum Jülich in Germany, an appropriate experimental set-up based on a dye laser pumped by an excimer laser has been prepared. Additionally, the system has been extended by a laser wavelength calibration facility in form of a helium glow discharge chamber. Section II describes these arrangements as well as the measurement strategy and typical signals are shown. In the section III, we explain these data analysis steps, which are necessary for the derivation of absolute populations of the excited levels and their comparison with model calculations: absolute helium amount in the fluorescence observation volumes, consideration of the Zeeman splitting of the pumped transitions and some other effects influencing the laser pumping efficiency. The next section (IV) deals with the modelling of atomic helium population distribution for a given set of n_e and T_e as well as the population perturbation of the relevant levels as a result of resonant laser interaction.

[*]Electronic address: Maciej.Krychowiak@ipp.mpg.de

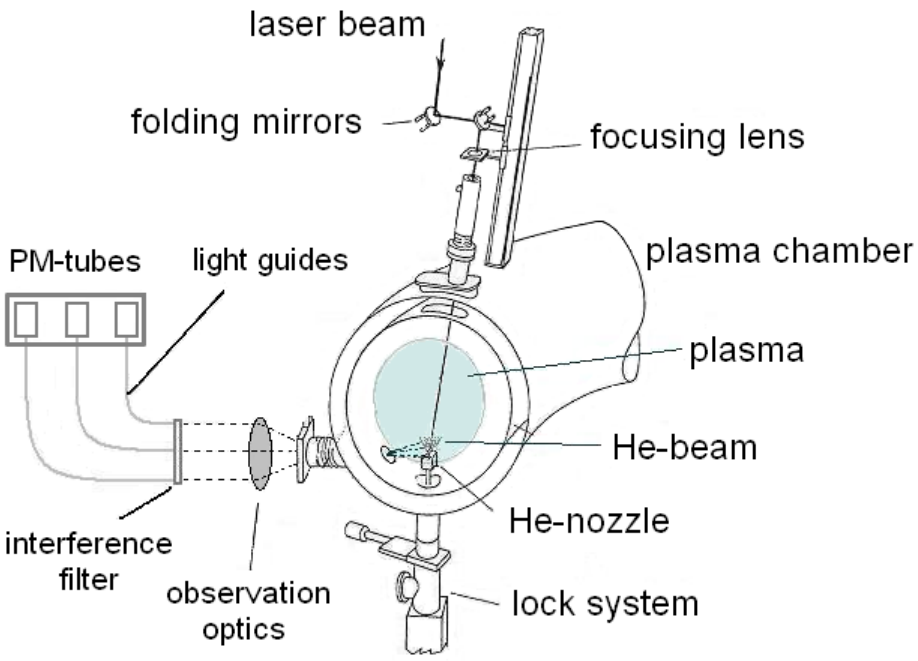

Figure 1: Experimental set-up of the LIF measurements on TEXTOR.

The simulations predict much larger signal-to-noise ratios for triplet pumping schemes and for this reason first measurements have been performed in the triplet system. Example results are presented in section V.

II. EXPERIMENTAL SET-UP

The measurements have been carried out on the TEXTOR tokamak. TEXTOR is a medium sized tokamak (major plasma radius $\mathrm{R}_0 = 1.75\,\mathrm{m}$, minor plasma radius $\mathrm{a} = 0.46\,\mathrm{m}$) with typical plasma current of $I_\mathrm{p} = 350\,\mathrm{kA}$ and magnetic field on the plasma axis of $B_\phi = 2.25\,\mathrm{T}$ [25, 26]. Ohmic heated discharges were used for experiments with line-averaged electron density in the range of $\overline{n}_\mathrm{e} = 2 - 4 \times 10^{19}\,\mathrm{m}^{-3}$. Constant plasma parameters can be sustained at TEXTOR within a plateau of typically 5 seconds. During this time, the laser wavelength is scanned over the expected spectral range of the excited transition (e.g. $\Delta\lambda \approx 70\,\mathrm{pm}$ for the triplet transition at $\lambda = 587.6\,\mathrm{nm}$) which is subject to Zeeman splitting owing to the presence of the strong (mainly toroidal) local magnetic field.

The laser radiation source is a two-stage system consisting of a pulsed excimer laser (Lambda Physik, type: LPX 315i) which pumps a dye laser (Sirah Laser- und Plasmatechnik, type: Double PrecisionScan). The system provides near ultraviolet to visible laser light with a spectral resolving power $\lambda/\Delta\lambda$ better than 10^5. The wavelength of the laser can conveniently be scanned (controlled via a remote PC) during the discharge time over a prescribed range with a given scan velocity. Laser pulses of 15 ns duration and maximum repetition frequency of 100 Hz provide energies of up to 60 mJ. In order to avoid unnecessary stray light and the effect of photoionisation, the maximum available laser energy was not generally utilised.

The laser beam is guided from the laboratory to the top of the tokamak by folding mirrors and directed down onto the gas nozzle (Figure 1). The laser light is initially linearly polarised. A $\lambda/2$ retardation plate is used to adjust the polarisation direction relative to the torus to coincide approximately with that of the magnetic field lines (excitation of the π components of the Zeeman spectrum). At the entrance of the beam into the machine, a focusing lens is used in order to produce at the nozzle position a sharp image of an iris which lets only the central part of the laser beam through. The diameter of the laser beam image at the nozzle is 2 cm.

The gas nozzle is mounted on a movable platform in a vacuum lock system [27]. This allows on the one hand the radial adjustment of the nozzle position and, on the other hand, calibration devices can be mounted instead of the nozzle making a reliable adjustment of the observation system possible without breaking the vacuum in the torus. Thermal helium atoms are radially injected through the nozzle into the plasma. The beam penetrates the plasma for several centimetres with a velocity of around 1.5 km/s and eventually vanishes due to ionisation losses [28]. The nozzle construction based on capillary tubes results in a beam divergence of around 40°.

The fluorescence light is observed perpendicularly to the torus and in the horizontal plane at three radial positions in the plasma

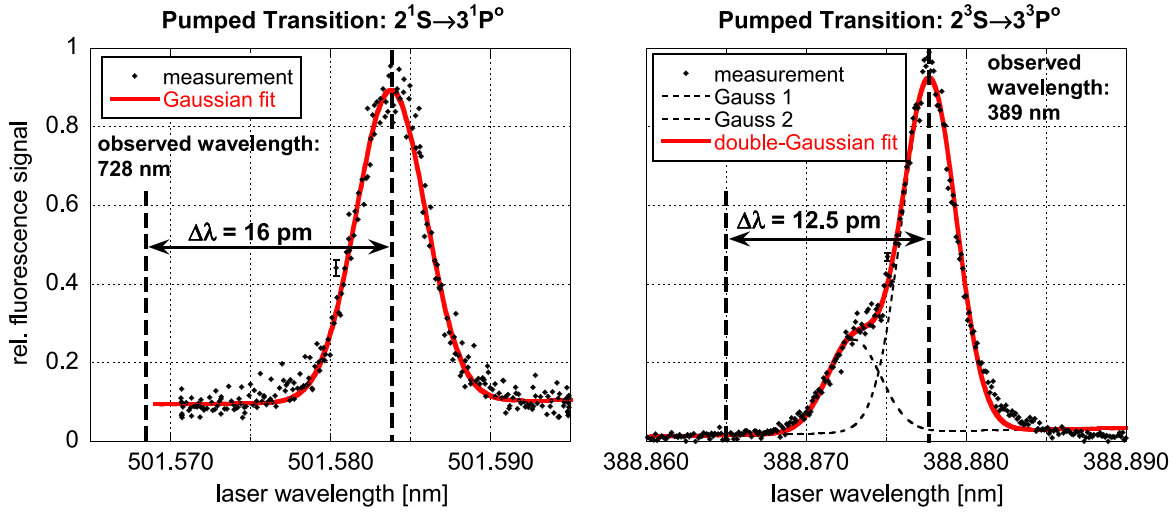

Figure 2: Fluorescence signals of two HeI transitions as measured for wavelength calibration purposes on a glow discharge set-up in the laboratory. Left: excitation of the singlet transition $2^1\mathrm{S}\rightarrow3^1\mathrm{P}^\mathrm{o}$ at $\lambda = 501.6\,\mathrm{nm}$ (fluorescence signal observed at $\lambda = 728.1\,\mathrm{nm}$, $3^1\mathrm{S}\rightarrow2^1\mathrm{P}^\mathrm{o}$). Right: excitation of the triplet transition $2^3\mathrm{S}\rightarrow3^3\mathrm{P}^\mathrm{o}$ at $\lambda = 388.9\,\mathrm{nm}$ (fluorescence signal observed at the same wavelength). $\Delta\lambda$ indicates a typical 'day-to-day' wavelength shift of the laser for experimental reasons.

simultaneously. This is equivalent to measurements at different pairs of $(n_\mathrm{e}, T_\mathrm{e})$. The observed volumes are imaged through an interference filter onto the entrance surface of fluid light guides with an inner diameter of 8 mm. The signals are detected by photomultiplier tubes and digitised by a fast acquisition device (1 GHz analogue bandwidth). The observation system has been carefully calibrated for absolute photon flux sensitivity at several wavelengths of helium lines to be observed by using of a broadband light source with a known spectral radiance (Ulbricht sphere VSS600 by LabSphere). During the calibration exactly the same optical as well as electrical set-up (including the high voltage on the photomultiplier tubes) is applied as during experiments to keep the uncertainty of the calibration procedure as low as possible. The system sensitivity has been also checked for its frequency response to ensure a proper interpretation of the short fluorescence light pulses. The linearity of the detectors has been investigated; nevertheless in some cases the laser stray light caused detector saturation. It was important to perform a proper spectral transmission versus wavelength calibration of the narrow-band interference filters ($\Delta\lambda = 1 - 2\,\mathrm{nm}$), since slight misalignment could easily result in a change in their transmission by a factor of two. The absolute calibration has been repeated a few times after a time period of typically several months to account for possible changes of the system sensitivity caused e.g. by the coating of the in-vessel optical components.

In order to compare the measured absolute populations with the results of the CR modelling we need to know the number of helium atoms in the observed fluorescence volume. This information is obtained from the helium flux through the nozzle, measured during test gas pulses with the same parameters as during experiments. Monitoring the gas pressure in the vacuum vessel during and after the gas puffs allows the determination of the time resolved total helium fluxes. These turn out to be nearly constant during the time window of constant plasma parameters for certain parameters of the gas puff.

The dye laser used may be affected by a certain wavelength shift which is not necessarily constant. To avoid a mismatch between the scanned wavelength range and the wavelength of the transition to be excited during relatively short TEXTOR plasma pulses of few seconds, a wavelength calibration of the laser system is carried out before each experimental unit (half a day). For this purpose a similar laser-induced fluorescence set-up on a glow discharge chamber has been prepared in the laboratory. The laser is spectrally fine-tuned to provide a fluorescence signal at any helium transition of interest in the glow discharge chamber. Sample measurements are shown in Figure 2. In the case of the singlet transition $2^1\mathrm{S}\rightarrow3^1\mathrm{P}^\mathrm{o}$ a single Gaussian profile fits the data, whereas when dealing with the triplet transitions, one has to consider their fine structure. The excited transition $2^3\mathrm{S}\rightarrow3^3\mathrm{P}^\mathrm{o}$ consists of three components, two of them lying close together (these cannot be resolved) and in a distance of $\Delta\lambda = 4.4\,\mathrm{pm}$ from the third component, which is enough to enable resolution with our laser. Two overlaid Gaussians fit the data very well, reflecting within 10% the separation of the components and their intensity ratio of $S_2/S_1 \approx 2.9$ which results from the statistical weights of the single sublevels of this multiplet and the fact of using strong, i.e. saturating laser radiation ($S_2/S_1 \approx (8/11)/(1/4)$). Finally, these measurements provide the wavelength offset of the dye laser, lying in the range of 10-30 pm and not being constant in the time, as well as the laser spectral width.

Figure 3 shows an example fluorescence signal as measured in TEXTOR at the laser wavelength of $\lambda = 587.6\,\mathrm{nm}$ ($2^3\mathrm{P}^\mathrm{o}\rightarrow3^3\mathrm{D}$). During 4 seconds of the plasma plateau (top figure) the laser wavelength has been scanned over a range of around 70 pm to cover the sets of σ^+ and π components of the Zeeman spectrum (bottom-right). A comparison with emission spectrum (bottom-left) calculated according to [29, 30] clearly shows good agreement. An additional scale has been provided to the plot

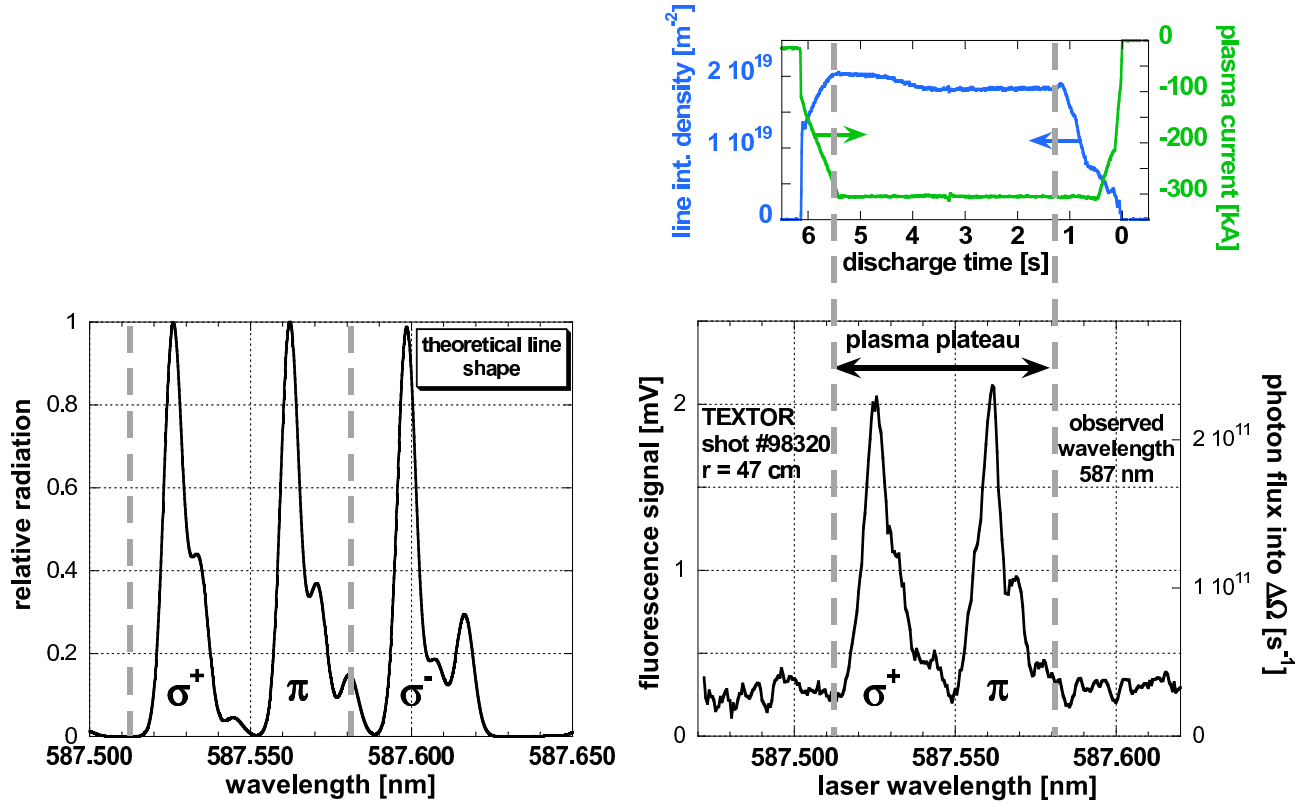

Figure 3: Bottom-right: fluorescence signal observed at the laser wavelength when exciting the triplet transition $2^3\mathrm{P^o}\rightarrow 3^3\mathrm{D}$ ($\lambda = 587.6\,\mathrm{nm}$) during a TEXTOR Ohmic discharge (σ^- missing owing to scanning range restricted on purpose); bottom-left: corresponding calculated Zeeman emission spectrum (B = 2.25 T assumed, as in experiment); top: plasma current and line integrated electron density during the discharge.

with the measured curve indicating the measured flux of fluorescence photons released from the observation volume into the solid angle of our observation system. From this photon flux the absolute population of the level pumped by the laser and further the population of this level relative to the ground state population is derived and compared with the CR model prediction (Figure 14).

III. EXPERIMENTAL DATA ANALYSIS

As already mentioned, we are interested in the measurement of the absolute populations of levels excited by laser light and in the comparison with model predictions. This requires some additional steps in terms of data analysis which are described in this section.

Firstly, we require the number of helium atoms in the fluorescence volume. The total helium flow (integrated flow rate) through the nozzle into the plasma is thus needed. It is determined by test gas puffs into the torus in the absence of plasma (see section II). In the second step, one has to consider the divergence of the atomic helium beam in the course of penetration into the plasma and its attenuation owing to ionisation losses. Since the theoretical description of these processes is difficult owing to several uncertainties, including that of the ionisation cross-section, an experimental determination is a better method.

For this purpose the line emission of atomic helium in the beam at the wavelength of $\lambda = 501.6\,\mathrm{nm}$ ($3^1\mathrm{P^o}\rightarrow 2^1\mathrm{S}$) is recorded by a 2D camera with an image intensifier by using the same observation port as for the fluorescence measurements. An example image is shown in Figure 4. The colour intensity in each pixel corresponds to the integral light emission along the line of sight of the camera i.e. in the poloidal direction. On integrating the signals over their extension in the toroidal direction (see Figure 4), one obtains a radial profile $I(r)$ of total light emission of the beam at the wavelength under consideration. It can be shown that this quantity is a measure of the ionisation losses – mainly from the ground state – of the beam [31, 32].

Our injection system delivers long gas pulses, the total gas flux of which can be assumed as constant on the relaxation time scale of the level populations. Thus, the partial time derivative of the (stationary) radial profile of ground state helium density $n_0(r)$ is equal zero and hence the ionisation losses are just balanced by the transport term:

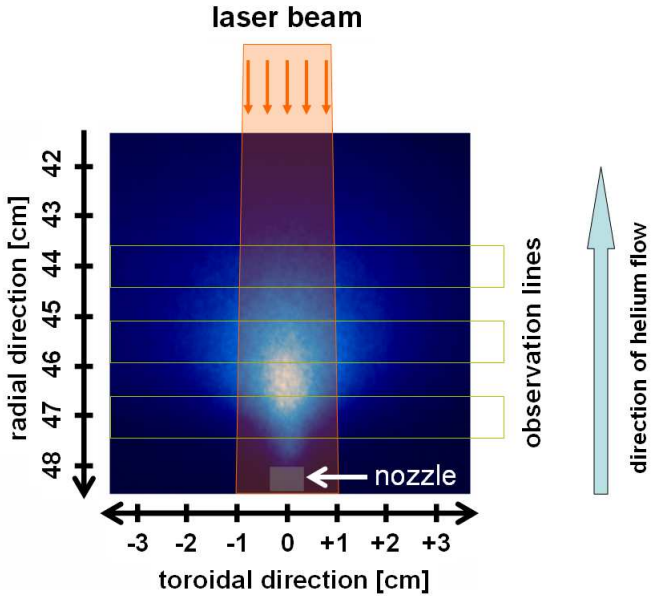

Figure 4: Beam emission at $\lambda = 501.6\,\mathrm{nm}$ ($3^1\mathrm{P^o}\rightarrow 2^1\mathrm{S}$) recorded with a 2D-camera during the flat-top phase of a discharge with $\overline{n}_\mathrm{e} = 4\times10^{19}\,\mathrm{m}^{-3}$. The path of the laser beam as well as the lines of sight are indicated.

$$\frac{\mathrm{d}n_0(r)}{\mathrm{d}t} = \frac{\partial n_0(r)}{\partial t} + v_\mathrm{He}(r)\frac{\partial n_0(r)}{\partial r} = S_\mathrm{ion}. \tag{1}$$

The ionisation loss term can be written

$$S_\mathrm{ion} = -n_0(r)\, n_\mathrm{e}(r)\, \langle \sigma_{0\rightarrow\mathrm{ion}} v_\mathrm{e}\rangle\,. \tag{2}$$

Upon insertion Eq. (2) in Eq. (1), one derives for the radial profile of the total (i.e. integrated over the poloidal and toroidal direction) ground state helium density in the beam the following expression:

$$n_0(r') = n_0(\mathrm{a}) - \int_\mathrm{a}^{r'} n_0(r)\, n_\mathrm{e}(r)\, \langle \sigma_{0\rightarrow\mathrm{ion}} v_\mathrm{e}\rangle \frac{\mathrm{d}r}{v_\mathrm{He}(r)}, \tag{3}$$

where a denotes the minor plasma radius. On the other hand the measured line intensity $I(r)$ from the level u corresponding to the local line emission coefficient can be written as

$$I(r) = \mathrm{const}\times n_0(r)\, n_\mathrm{e}(r)\, \langle \sigma_{0\rightarrow\mathrm{u}} v_\mathrm{e}\rangle\,, \tag{4}$$

assuming that the radiating level u is populated mainly by electron collision-induced transitions from the ground state and its most important depopulation channel is spontaneous radiation (both assumptions are justified for the observed transition, see also Figure 6). Replacing in Eq. (3) the expression for $n_0(r)\, n_\mathrm{e}(r)$ derived from Eq. (4) yields:

$$n_0(\mathrm{a}) - n_0(r') \propto \int_\mathrm{a}^{r'} I(r) \frac{\langle \sigma_{0\rightarrow\mathrm{ion}} v_\mathrm{e}\rangle}{\langle \sigma_{0\rightarrow\mathrm{u}} v_\mathrm{e}\rangle} \frac{\mathrm{d}r}{v_\mathrm{He}(r)}. \tag{5}$$

While there is thus no direct electron density dependence in this expression, the electron temperature dependence of the rate coefficients remains. Since both collisional rate coefficients appearing in Eq. (5) have a similar temperature dependence in the range 10-100 eV, their ratio can be extracted from the result of the radial integration. Furthermore, if assuming a radially constant (negative) velocity $v_\mathrm{He}(r) = \mathrm{const} < 0$ of the beam (see the direction of the beam flow in Figure 4), the profile of the particle losses is obtained simply by integration of the measured light intensity from the plasma edge to the considered radial point r':

$$n_0(\mathrm{a}) - n_0(r') \propto -\int_{\mathrm{a}}^{r'} I(r)\mathrm{d}r. \tag{6}$$

Results of such an integration are shown in Figure 5. One can see that the amount of fluorescence signal at the innermost channel will be more than a factor of three smaller than at the channel at $r = 47\,\mathrm{cm}$ owing to ionisation losses alone.

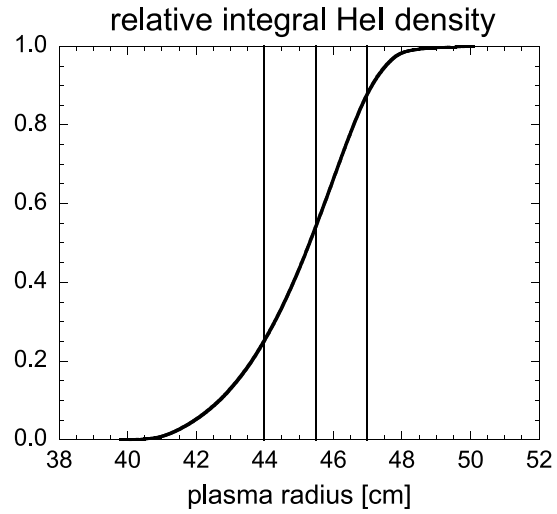

Figure 5: Attenuation of the helium beam in the course of the plasma penetration due to ionisation losses derived by integrating of the beam emission shown in Figure 4 according to Eq. (6). Indicated are the three radial positions of our fluorescence measurements (see also Figure 1).

As a test of the justification of the assumptions described above which allow the use of line emission from the level $3^1\mathrm{P^o}$ as a measure of the local ionisation loss rate, the attenuation of the ground state population $n_0(r)$ of a sample beam penetrating a plasma of given parameters as well as the time derivative $\mathrm{d}n_0/\mathrm{d}t$ are calculated by the CR model. As we see in Figure 6 the derivative curve (dashed blue line) expressing the ionisation losses coincides well with the emission from the level $3^1\mathrm{P^o}$ (solid red line) which is not the case for the other plotted emission curves.

The second factor which also results in the reduction of the local helium density in the beam is beam divergence. It is allowed for in such a way that the local helium density profile $n_{\mathrm{He}}^{\mathrm{loc}}(\tilde{r})$ around the beam axis for a given radial position in the plasma r' is assumed to have circular symmetry ($n_{\mathrm{He}}^{\mathrm{loc}}(\tilde{r} = \mathrm{const}) = \mathrm{const}$). Since the signals recorded by the camera are line integrated

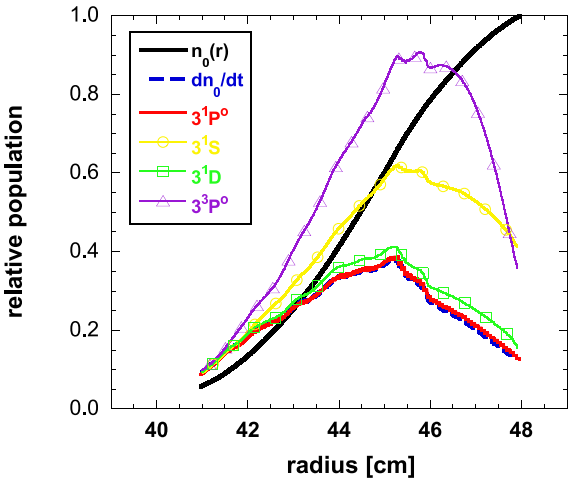

Figure 6: Test of the assumptions made for the derivation of Eq. (6). The CR model calculation of the line emission from the level $3^1\mathrm{P^o}$ (solid red line) coincides well with the time derivative (dashed blue line; ionisation losses) of the calculated ground state density profile (solid black line). Emission from other levels (remaining curves) cannot be used for this purpose. (All coloured curves are rescaled and shifted to coincide at $r = 41\,\mathrm{cm}$.)

intensities in the poloidal direction, any toroidal profile of the measured intensity at a desired plasma radius r' can be easily Abel-inverted according to [33]

$$n_{\mathrm{He}}^{\mathrm{loc}}(\tilde{r}) = -\frac{1}{\pi}\int_{\tilde{r}}^{\tilde{R}} \frac{\mathrm{d}I(y)}{\mathrm{d}y}\frac{\mathrm{d}y}{\sqrt{y^2-\tilde{r}^2}}, \tag{7}$$

yielding the local helium density (y denotes the variable of integration, and $\tilde{R}$ the maximum distance from the beam axis to the point where the helium light was still detected). Integration is performed for all three radial positions r' of our observation channels accounting for their radial extension as indicated in Figure 4. One example is shown in Figure 7.

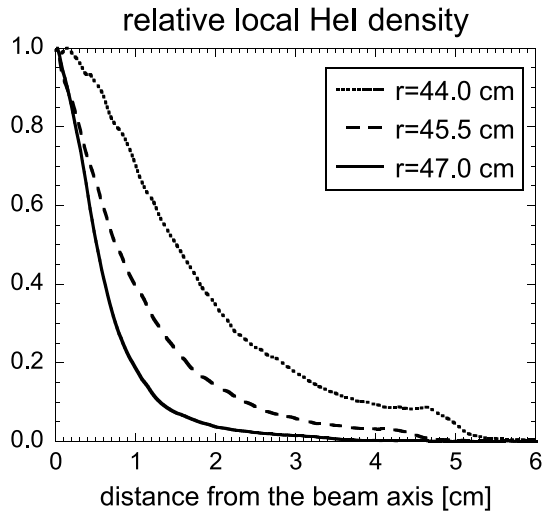

Figure 7: Relative local helium density around the beam axis for three radial positions of our observation system as derived by Abel inversion of the corresponding toroidal profiles from the camera measurement.

The local density profile can now be integrated over the area where the laser beam and the path of the line of sight overlap. This provides, together with the beam attenuation profile and the helium flux through the nozzle, the number of atoms the fluorescence light of which contribute to the measured signal. It turns out that even at the outermost observation position only about 25% of the initial beam content is effectively used for the measurements.

Scanning the laser wavelength over the Zeeman spectrum of the pumped transition yields the maximum fluorescence signal which can be then compared to the calculated one. Unfortunately the small spectral width of our dye laser does not permit coverage of all Zeeman components. This is unfortunate, since the present procedure results in a loss in intensity and makes comparison with calculated signals harder, especially in the case of triplet transitions, because of its fine structure. In fact, in the example of the triplet transition $2^3\mathrm{P^o}\rightarrow 3^3\mathrm{D}$ ($\lambda = 587.6\,\mathrm{nm}$), the laser cannot even cover all components of the set of the π lines (Figure 8 to be compared with Figure 3 below). This complicates the determination of the fraction of the $2^3\mathrm{P^o}$ level population which is being pumped to the upper level, even in the simpler case of saturating laser power.

In Figure 8, the transition probabilities (A-values) of all Zeeman components of the transition $3^3\mathrm{D}\rightarrow 2^3\mathrm{P^o}$ are plotted against wavelength. Owing to partial overlap, fewer than 40 components are apparently visible. The π and σ components have been colour-coded separately. The nine dominant π components in the wavelength range of $587.5600 - 587.5807\,\mathrm{nm}$ have been listed separately in Table I. These have been taken into account in the calculation of the population fraction of the $2^3\mathrm{P^o}$ level pumped to the upper level.

Figure 9 shows the Zeeman-split transition $3^3\mathrm{D}\rightarrow 2^3\mathrm{P^o}$ in form of a Grotrian diagram. Only the nine dominant π components are indicated. As shown, the corresponding transitions connect all nine magnetic sublevels of the lower level with nine different sublevels of the upper level (marked with bold lines). This means that a saturating unpolarised broadband laser spectrally covering only all the π transitions would be able to transfer one half of the lower population to the upper level (in the case of a laser spectrally covering all π and σ components this pumping efficiency would climb to $15/24$). These fractions, as indicated, apply provided that the initial populations of the upper magnetic sublevels are negligibly small, and that these sublevels remain collisionally decoupled, i.e. provided that collisional population transfer between them may be neglected over the time-scale of the laser pulse. Such instant mixing is equivalent to the excitation along all transitions of the Zeeman structure resulting in an increased value of the pumped fraction to $15/24$ and of the upper level population in the presence of laser light. Consequently, collision-induced signals would become larger. In contrast, changes in the polarisation of the fluorescence light from the upper level counteract the increasing pumped fraction so that fluorescence intensities at the laser wavelength observed perpendicularly to the strong magnetic field in the case of saturating laser power remain approximately unchanged when pumping

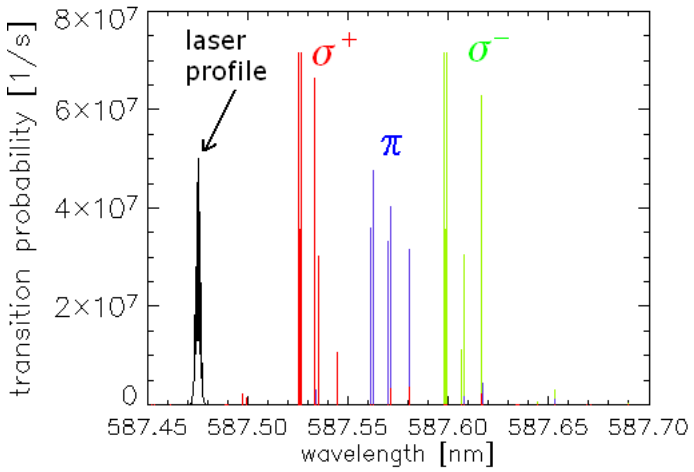

Figure 8: Zeeman components of the transition 3^3D→2^3P^o at $\lambda = 587.6\,\mathrm{nm}$ calculated for B = 2.25 T. π and σ components are plotted in different colours. For comparison the laser profile is superimposed.

J_u	m_u	J_l	m_l	wavelength [nm]	A_i [$10^8 s^{-1}$]	p_i
3	0	2	0	587.5700	0.333	1.12
3	-1	2	-1	587.5626	0.477	1.25
3	-2	2	-2	587.5615	0.358	1.12
2	2	2	2	587.5615	0.358	1.12
2	1	2	1	587.5622	0.358	1.12
2	0	1	0	587.5714	0.403	1.25
2	-1	1	-1	587.5624	0.358	1.12
1	1	1	1	587.5626	0.477	1.25
1	0	0	0	587.5807	0.316	1.12

Table I: The nine dominant π components of the transition 3^3D→2^3P^o at $\lambda = 587.6\,\mathrm{nm}$ (calculated for B = 2.25 T) which are taken into account for calculation of the 2^3P^o population fraction pumped to the upper level. The wavelengths, the A-values as well as the effective polarisation factors are shown.

the π transitions (for the transition $2^3\mathrm{S} \rightarrow 3^3\mathrm{P}^o$ it can be shown that the polarisation effect exactly counteracts the increased pumped fraction and hence the fluorescence signal at the laser wavelength is independent of the degree of the collisional mixing).

The effect of collisional population transfer between magnetic sublevels was observed in a hollow cathode discharge by Takiyama et al. [34, 35]. However, it was attributed to atom-atom collisions due to high atomic gas density in the range of $n_{\mathrm{He}} \sim 10^{16}\,\mathrm{cm}^{-3}$. In our case electron or, owing to the small energy differences of the magnetic sublevels, more likely proton collisions could be sufficiently rapid for the redistribution (see also the discussion on the statistical population of hydrogen fine structure levels for typical fusion edge plasma parameters in [36]). Since no rate coefficients for the collisional population transfer between the magnetic sublevels are known, we neglect this effect in the calculation. This question could be examined experimentally by measurement of time-resolved traces of both π and σ components (to be separated by their polarisation) of the resonant fluorescence light in the case of exciting e.g. only a π component. Detection of spectrally resolved components failed due to the too low sensitivity of the gated high-resolution spectrometer.

The above considerations and assumptions permit the calculation of the approximate lower level population fraction pumped to the upper level as a function of the laser wavelength. The only additional input needed here is the spectral width of a single absorption line which is most strongly affected by the Doppler broadening depending on the helium temperature in the beam. For this temperature we assume a first wall (liner) temperature of 180°C. With a laser pulse of a given spectral width in the example of the transition 3^3D→2^3P^o it is sufficient to separately calculate this fraction for each Zeeman transition since all the transitions connect nine different sublevels of both the lower and the upper level (Figure 9). The difficulty is that the laser pulse provides saturation of the pumping process more or less in the centre of its spectral profile. The contribution of the spectral wings of the laser profile to the pumping efficiency is therefore lower. Additionally the laser profile deviates from a Gaussian. In order to allow for these effects we simulate the pumping efficiency with a computer code. These simulations are performed

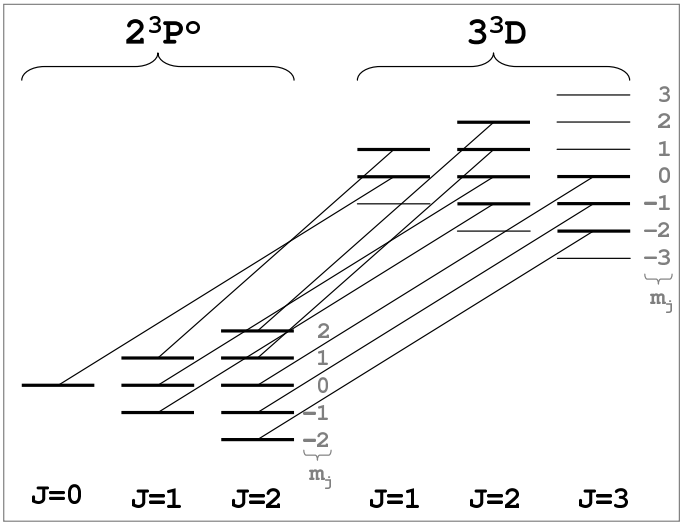

Figure 9: Part of the Grotrian diagram of HeI showing the Zeeman structure of the transition $3^3\mathrm{D}\rightarrow 2^3\mathrm{P}^\mathrm{o}$ at $\lambda = 587.6\,\mathrm{nm}$. Only those transitions are indicated which are listed in Table I, and correspond to the nine dominant π components of the line.

for a whole series of laser pulses stepping across the spectrum with incremental changes of the central wavelength of the laser profile, just as in the experiment.

As a result, a spectrum of the pumping efficiency is obtained. However, it cannot be directly compared to the measured signals. This is because the observed fluorescence light (separated from the plasma radiation by interference filters with the spectral width of $\Delta\lambda \sim 1\,\mathrm{nm}$) differs in the degree of polarisation (p_i), depending on the upper sublevel i it originates from. We have to keep in mind that due to the finite width of the interference filters the detected fluorescence radiation consists not only of the π lines, which are excited but also of additional (mostly) sigma lines. The polarisation dependent factors for our observation angle of $\sim 90^\circ$ with respect to the magnetic field, by which the over the whole space 4π integrated A-values have to be multiplied, are 3/2 and 3/4 for the π and the σ lines, respectively. The final p_i values are obtained by weighting the factors 3/2 and 3/4 with the corresponding A-values for the π and σ lines. They are listed in Table I. The resulting spectrum – including the polarisation effect – can be then compared with the experimental spectrum of the fluorescence signals. The signal amplitudes provide a comparison of the absolute population density of the lower level. On the other hand, the comparison of the widths of the spectra can be utilised to cross-check the assumed spectral widths of the laser profile and absorption lines. In the case of a more complicated spectrum than e.g. of only a single Gaussian profile, the reconstruction of the features of the profile serves as an additional check for the proper simulation procedure.

Figure 10 shows a measured relative fluorescence spectrum with an overlaid simulated spectrum of the π components. The scaling of the y axis refers to the simulation curve. The y values are the transition probabilities for the total radiation from the upper sub-levels weighted with their relative population increase Δn_i due to laser pumping and the polarisation factors p_i (n_i denotes the initial lower level population). At the maximum ($\lambda = 587.562\,\mathrm{nm}$) the calculated pumped fraction of the lower level population amounts to around 1/2 of the maximum which would be achievable with a broadband laser. The slight flattening at the maximum of the measured profile may be due to approaching detector saturation.

IV. COLLISIONAL-RADIATIVE MODEL CALCULATION

For the prediction of the fluorescence signals on TEXTOR we use a code which is a slightly modified form of the time-dependent CR model code used as the basis for the derivation of the electron density and temperature from the measured line intensity ratios [1, 2, 37]. In order to obtain the stationary ($\frac{\partial n_i}{\partial t} = 0$, see Eq. (1)) population density profile $n_i = n_i(r)$ of the *i*th quantum level of helium atoms in the beam in the absence of the laser pumping beam, the population and loss processes of all 29 included levels of the shells $n = 1 - 5$ need to be balanced by the transport term

$$\sum_{j\neq i} \langle\sigma_{j\rightarrow i} v_\mathrm{e}\rangle\, n_\mathrm{e} n_j - \sum_{j\neq i} \langle\sigma_{i\rightarrow j} v_\mathrm{e}\rangle\, n_\mathrm{e} n_i + \sum_{j>i} \mathrm{A}_{j\rightarrow i} n_j - \sum_{j<i} \mathrm{A}_{i\rightarrow j} n_i - \langle\sigma_{i\rightarrow\mathrm{ion}} v_\mathrm{e}\rangle\, n_\mathrm{e} n_i = v_\mathrm{He}(r) \frac{\partial n_i(r)}{\partial r}. \qquad (8)$$

The left hand side of the above equations includes the electron collisions (excitation and deexcitation), spontaneous decay and the population losses caused by ionisation (more details about the rate parameters included in the model are given in [38]). To

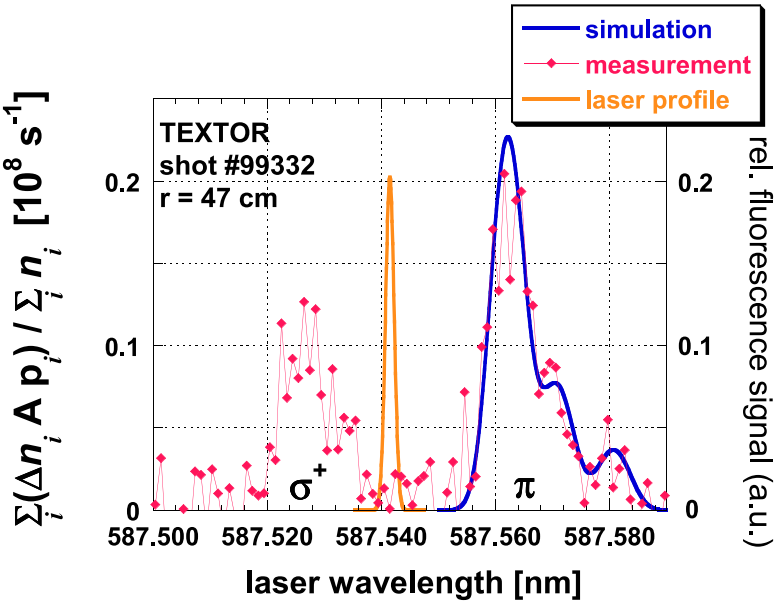

Figure 10: Calculated and measured fluorescence spectra at the laser wavelength $\lambda = 587.6\,\mathrm{nm}$ for the case where the transition $2^3\mathrm{P^o}\rightarrow 3^3\mathrm{D}$ is pumped. The π components alone have been fitted. For comparison the scanning laser profile is added.

solve the set of equations we change to the coordinate system moving with the beam velocity v_{He} by $\frac{\partial r}{\partial t} = v_{\mathrm{He}}$. Thus the equations transform to a set of time dependent equations where the coefficients carry the time dependence through the space dependence, e.g. $T_{\mathrm{e}}(r) = T_{\mathrm{e}}(r(t))$ with $\frac{\mathrm{d}r}{\mathrm{d}t} = v_{\mathrm{He}}$. The result can then be transformed back to space coordinates by the inverse transformation. The system of 29 differential rate equations is solved numerically by using the step width controlled Runge-Kutta method. Initial populations are set to one for the ground state and zero for all excited levels.

When looking for a stationary population distribution at a certain radial position with an electron density not too low ($n_{\mathrm{e}} \gtrsim 2\times 10^{12}\,\mathrm{cm}^{-3}$) an additional assumption to the beam stationarity can be made, significantly simplifying the model calculation: The relaxation times of all excited levels become sufficiently short so that, when considering the level populations relative to the ground state population ($n_i^{\mathrm{relat.}} = n_i/n_0$), their radial transport can be neglected (i.e. $v_{\mathrm{He}}\frac{\partial}{\partial t} n_i^{\mathrm{relat.}} \approx 0$). The relative populations of excited levels are then achieved for the given radial position as the steady state distribution. This quasi-steady state solution can then be calculated much faster by simple matrix inversion [2].

The stationary solutions of the population distribution are used as the starting point for investigating the influence of the pulsed resonant laser radiation on the level populations. Since the laser pulse length ($\mathrm{T_L} \sim 15\,\mathrm{ns}$) and the relaxation times of the excited levels ($\tau_{\mathrm{relax}} \sim 100\,\mathrm{ns}$, see Figures 11 and 12) are short we can neglect the transport term again in the analysis. To include the laser pulse we simply extend the left side of Eqs. (8) with four terms reflecting the stimulated transition rates (excitation and decay) as sources and sinks of the population of both levels u and l involved in the laser pumping process:

$$\begin{aligned} \tfrac{\partial n_{\mathrm{u}}}{\partial t} &= \ldots + \rho \mathrm{B_{l\rightarrow u}} n_{\mathrm{l}} - \rho \mathrm{B_{u\rightarrow l}} n_{\mathrm{u}} \\ &\qquad , \quad \rho > 0 \ \text{ for } \ \Delta t = \mathrm{T_L}. \\ \tfrac{\partial n_{\mathrm{l}}}{\partial t} &= \ldots + \rho \mathrm{B_{u\rightarrow l}} n_{\mathrm{u}} - \rho \mathrm{B_{l\rightarrow u}} n_{\mathrm{l}} \end{aligned} \qquad (9)$$

ρ is the spectral power density of the laser radiation and B are the Einstein coefficients for absorption and induced emission. The time development of the perturbation is obtained from 29 equations for the partial time derivatives $\frac{\partial n_{\mathrm{i}}}{\partial t}$. We approximate the temporal profile of the laser power with a rectangular function. Similar simulations with emphasis placed on the impact of variation of rate coefficients for the collisional transfer between the $n = 3$ levels on the fluorescence signals can be found in [39].

Figure 11 shows an example of such a calculation for $n_{\mathrm{e}} = 5\times 10^{12}\mathrm{cm}^{-3}$ and $T_{\mathrm{e}} = 50\,\mathrm{eV}$. The selected laser wavelength of $\lambda = 587.6\,\mathrm{nm}$ corresponds to the triplet transition $2^3\mathrm{P^o}\rightarrow 3^3\mathrm{D}$. The laser pulse energy of 0.2 mJ is sufficient for the saturation of the pumping process. This becomes evident through the instantaneous increase of the 3^3D population to its maximum after switching on the laser at t = 10 ns as well as through the constant population ratio of the upper and the lower level (3^3D and $2^3\mathrm{P^o}$) during the laser pulse. Since for this calculation a broadband laser has been assumed this constant ratio is equal to the ratio of the statistical weights (15/9). In fact, however, the pumping process is less efficient, since the spectral width of the laser line falls below the energy spread in the lower level resulting from the Zeeman splitting. A lower population ratio is thus produced

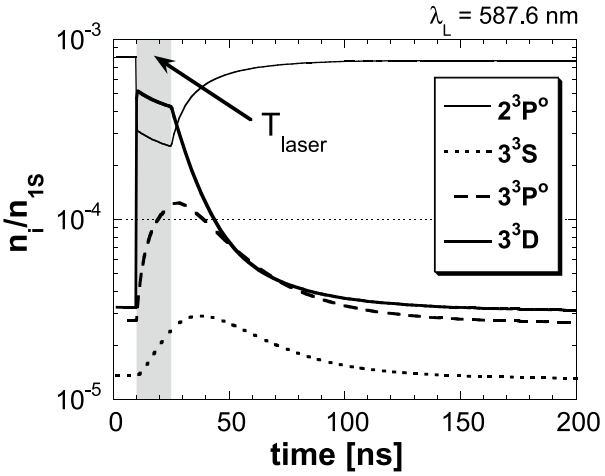

Figure 11: The influence of resonance laser radiation with wavelength $\lambda = 587.6\,\mathrm{nm}$ on the populations of selected triplet levels (relative to the ground state). A broadband saturating laser radiation has been assumed, and the Zeeman effect neglected.

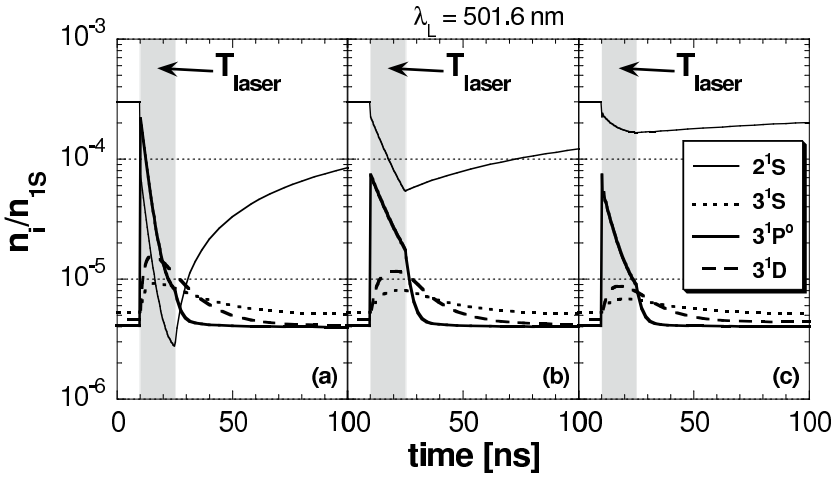

Figure 12: Impact of the resonant laser radiation at $\lambda = 501.6\,\mathrm{nm}$ on the population of selected singlet levels (relative to the ground state) calculated with the code based on the CR model for atomic helium; (a): Broadband saturating laser radiation has been assumed, the Zeeman effect is neglected; (b): Real case of a narrow-band laser assumed, and the Zeeman effect is accounted for; (c): Additional correction due to strong radiative losses from the level $3^1\mathrm{P^o}$ is introduced (see explanation in the text).

at saturation than for the example shown in Figure 11 (see also section III). Taking into account the observation geometry and helium density in the beam, one can calculate from this population the expected fluorescence response for the experiments on TEXTOR. Its deviation from the measured signal suggests certain weaknesses of the model calculation.

Figure 11 also shows a decreasing population of both levels optically involved in the laser pumping process during the laser pulse as well as the increasing population of the other two $n = 3$ triplet levels with some time delay. This is due to collisional population transfer from 3^3D to $3^3\mathrm{P^o}$ and from $3^3\mathrm{P^o}$ to 3^3S as indicated in Figure 13. Fluorescence radiation in the visible or near UV spectral range from these levels could be detected as well under some conditions, enabling a check to be made via the simulation procedure of the assumed collisional rate coefficients between the $n = 3$ levels.

Another calculation example is depicted in Figure 12. In this case the laser light at $\lambda = 501.6\,\mathrm{nm}$ pumps the transition $2^1\mathrm{S}\rightarrow 3^1\mathrm{P^o}$. In all three cases the upper level population increases instantly after switching on the laser, owing to the strong laser power. The constant population ratio of the upper and the lower level during the laser pulse in case (a) is again equal to the ratio of their statistical weights ($\mathrm{g_u/g_l} = 3/1$) since a broadband laser has been assumed and the Zeeman effect neglected. In contrast to the pumping scheme shown in Figure 11 the instantaneous population increase of the upper level is followed by rapid depopulation arising from the very rapid radiative channel from level $3^1\mathrm{P^o}$ to the ground state. This makes the detection of the fluorescence signal at the laser wavelength very difficult, when additionally considering the spurious impact of the scattered laser light.

In case (b) a realistic laser spectral width of around half of the width of the absorption line is assumed such that only half of

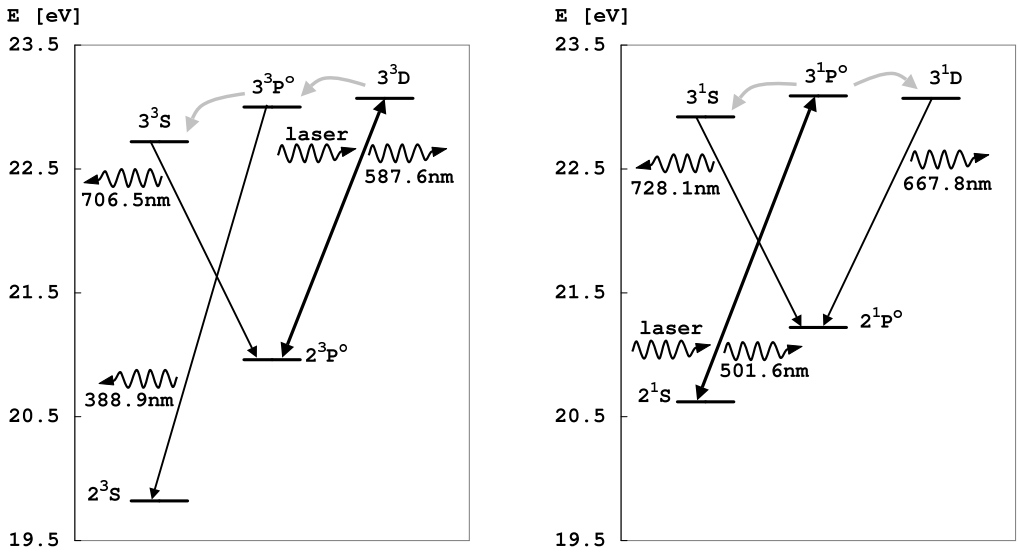

Figure 13: Pumping channels for the simulations as shown in Figures 11 and 12. The grey arrows represent the collisional population transfer between the $n = 3$ levels.

the lower level population is subject to the laser interaction. This leads, on the assumption that $g_{\rm l} = g_{\rm u} = 1$ (in accordance with the Zeeman effect) to a quarter of the initial lower level population being pumped to the upper level. This can be incorporated in the simulation by introduction of effective statistical weights for the upper and lower level, for the duration of the laser pulse, of $\rm g_l = 3$ and $\rm g_u = 1$. However, in that special case of a strong radiative decay of the upper level during the laser pulse, this treatment causes a considerable error in the calculation. Due to the strong radiative losses of the upper level and due to the constant population ratio of the upper to the lower level enforced by the saturating laser power, the lower level 2^1S serves as a population reservoir for the upper level. Its initial population drops almost to zero in case (a) and more than a factor of five in case (b). However, in case (b) only a half of the lower level population experiences the laser impact (serves as reservoir) and for this reason its initial population cannot drop below the mark of 50%. This can be reconstructed in the simulation by setting the laser stimulated excitation rate proportional to the remaining reservoir population rather than to the total lower level population. The result is shown in Figure 12 (c): the lower level population does not fall below 50% of its initial value and as consequence the upper level is depleted even faster than in case (b) which finally adversely affects the expected fluorescence response at all three wavelengths.

Owing to the existence of the ground state in the singlet system, pumping schemes based on triplet transitions are expected to provide much stronger fluorescence signals. This is the reason why we started our measurements with the triplet transitions.

V. FIRST RESULTS

Experiments on TEXTOR have been carried out with the laser at $\lambda = 388.9\,\rm nm$ and $\lambda = 587.6\,\rm nm$ pumping the triplet transitions 2^3S→3^3P$^{\rm o}$ and 2^3P$^{\rm o}$→3^3D, respectively (see Figures 13 left and 15). Figure 14 shows the measured absolute populations of the lower levels 2^3S and 2^3P$^{\rm o}$ obtained at two radial observation positions ($r = 47$ and $r = 45.5$ cm) during several ohmic discharges. They are given as population densities relative to the ground state population to be directly compared with the CR model calculations. The measured populations of the triplet metastable 2^3S lie below the model prediction, in the range of 0.5-0.95 of that and within the error bars (these are mainly due to the scattered laser light as well as due to the uncertainties in the derivation of the pumping efficiency, helium concentration in the observation volume and the absolute calibration factors). A similar result of 0.4-0.7 of the model prediction is obtained for the relative population of the level 2^3P$^{\rm o}$ except for two measurement points. The lower populations resulting from measurement cannot be explained by resonant reabsorption of line radiation by helium atoms in the beam (optical thickness). The maximum helium density at the beam axis was too low to alter considerably even the singlet metastable population by reabsporption by the ground state atoms. The effect of the radial transport of the triplet metastables 2^3S for lower electron densities ($n_{\rm e} \lesssim 2 \times 10^{12}\,\rm cm^{-3}$) (see section IV) is taken into account in the model calculation shown in Figure 14. The detailed analysis of possible model corrections explaining the discrepancies were described elsewhere [38].

In another experiment the fluorescence light has been detected at all three wavelengths (according to the $n = 3$ triplet levels as indicated in Figure 15) upon the laser excitation of the triplet transition 2^3S→3^3P$^{\rm o}$ at $\lambda = 388.9\,\rm nm$. Figure 16 shows the time

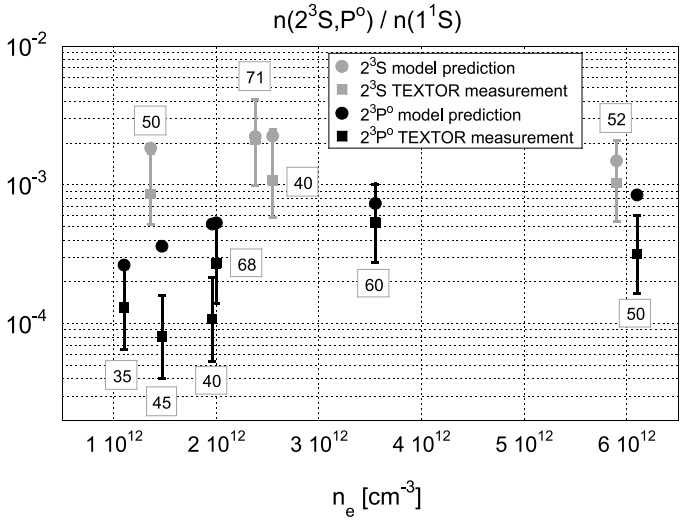

Figure 14: Results of the model calculation and measurement of the 2^3S and 2^3P^o population (relative to the ground state population). The corresponding electron temperatures are given in boxes.

traces of the signals as measured at the radial position $r = 47\,\mathrm{cm}$ with the plasma parameters, taken from similar discharges: $n_\mathrm{e} = 1.35 \times 10^{12}\mathrm{cm}^{-3}$ and $T_\mathrm{e} = 50\,\mathrm{eV}$. A remarkable difference is observed in the noise level of the measurement in case (c) versus cases (a) and (b). The highest signal-to-noise ratio could be expected in the case (b) of the fluorescence at the laser wavelength. However, a strong laser stray light – being subtracted by recording the laser pulses without plasma – blinds the observation system deteriorating the signal quality. The higher level of noise at $\lambda = 706.5\,\mathrm{nm}$ (plot (a)) compared to the signal at $\lambda = 587.6\,\mathrm{nm}$ (plot (c)) results from the lower transition rate for the collisional transfer from the level 3^3P^o to 3^3S than to 3^3D, the lower radiative decay probability from the level 3^3S than 3^3D as well as from a lower detector sensitivity at $\lambda = 706.5\,\mathrm{nm}$ than at $\lambda = 587.6\,\mathrm{nm}$.

The signal decay shapes of the three curves depend among other things on the well known radiative decay probabilities. Since the electron density is high enough to induce a population transfer from the level 3^3P^o to 3^3S and 3^3D all three signals will also depend on the electron density and the transfer rate coefficients. In particular the signals in case (a) and (c) depend mainly only on one rate coefficient: the one for collisional transfer from the level 3^3P^o to 3^3S and 3^3D, respectively. This provides a possibility for the determination of both rate coefficients if the electron density is known, particularly interesting in case (c) in which the high signal purity allows the determination of the rate coefficient with relatively high precision. In Figure 16 (c) we see that the time trace calculated with the unchanged CR model (black line) decays too slowly. In red the best fit of the measured time trace in plot (c) is indicated which required a higher value, than in our standard model, of the rate coefficient $\langle\sigma v\rangle_{3^3\mathrm{P^o}\rightarrow 3^3\mathrm{D}}$ by a factor of 1.57 (the rate coefficient $\langle\sigma v\rangle_{3^3\mathrm{P^o}\rightarrow 3^3\mathrm{S}}$ is chosen 1.4 times higher which follows from the ratio of both rate coefficients obtained from the maximum measured signal amplitudes in plots (a) and (c); the enhanced value of $\langle\sigma v\rangle_{3^3\mathrm{P^o}\rightarrow 3^3\mathrm{S}}$ has, however, no impact on the simulated time trace in plot (c)). The blue curves are simulation results in which the rate coefficient $\langle\sigma v\rangle_{3^3\mathrm{P^o}\rightarrow 3^3\mathrm{D}}$ was additionally lowered just by the factor which results in an unsatisfactory fit in plot (c). The factor amounts to 15% and hence this is about the accuracy of the rate coefficient, provided all other parameters are known.

On the other hand, once the rate coefficient $\langle\sigma v\rangle_{3^3\mathrm{P^o}\rightarrow 3^3\mathrm{D}}$ has been measured with sufficient accuracy, the decay of the fluorescence signal at $\lambda = 587.6\,\mathrm{nm}$ following a laser pulse at $\lambda = 388.9\,\mathrm{nm}$ could possibly be used to derive the local electron density (n_e measurements in low temperature plasmas have been reported, either from a ratio of time integrated (laser- and collision-induced) fluorescence signals [40, 41] or from the time trace of the collision-induced signals at $\lambda = 388.9\,\mathrm{nm}$ after a laser excitation at $\lambda = 587.6\,\mathrm{nm}$ [42]). The convenience of this LIF-based measurement when comparing to absolute population determination is that only relative fluorescence signals are needed (no absolute calibration of the observation system necessary; exact laser adjustment not crucial). Moreover, the laser-perturbed populations of the relevant levels return to their initial values after a few hundred nanoseconds and the system is in principle ready for the next sample after this short time period. A sensitivity analysis of such a measurement is possible using our modified CR code and is ongoing.

VI. SUMMARY

The use of passive line radiation of atomic helium in a plasma for derivation of spatially and temporally resolved electron density and temperature relies on the quality of the collisional-radiative model which is needed for the data analysis of those

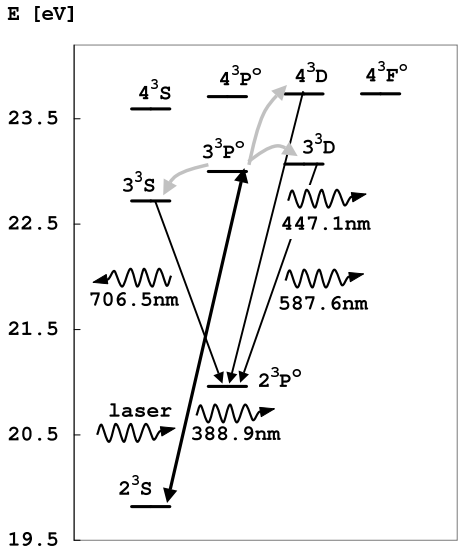

Figure 15: Pumping scheme for the measurements as shown in Figure 16. The grey arrows represent the collisional population transfer between the levels of the shell $n = 3 - 4$.

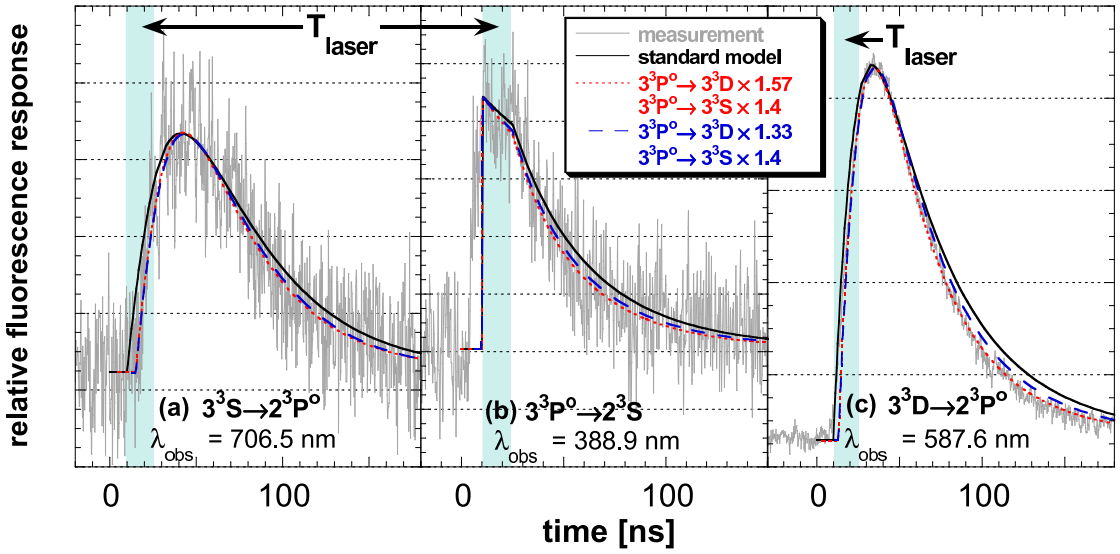

Figure 16: Time traces of relative fluorescence signals induced by laser pulses at $\lambda = 388.9\,\mathrm{nm}$ measured at three different wavelengths (originating from all three $n = 3$ triplet levels, see Figure 15). Results of the model calculation at enhanced values of two rate coefficient are included.

helium-based diagnostics. The laser-induced fluorescence method, as presented in this paper, allows the validation of some parameters and predictions of this model. Near ultraviolet and visible laser light can be used to excite helium atoms from the levels with $n = 2$ providing information about their population. To obtain their absolute populations, additional analysis steps have to be performed, including the assessment of the helium concentration in the fluorescence volume as well as the investigation of the laser pumping efficiency. The latter depends upon several processes, e.g. the Zeeman splitting of the pumped transition due to magnetic field. First measurement results show a somewhat lower population of the triplet levels 2^3S and 2^3P^o than predicted by our collisional-radiative model. The possible reasons for that were discussed in [38]. Furthermore, a direct method for measurement of the rate coefficients for collisional transfer between some levels with $n = 3 - 4$ is possible when analysing time traces of (collision-induced) fluorescence signals originating from other levels than those populated by the resonant laser. One example of such a measurement in a triplet pumping arrangement has been presented showing a feasibility of electron density derivation from collision-induced fluorescence signals. A further analysis of the collision-induced signals will allow the validation of the rate coefficients for collisional transfer between the excited levels and possibly change the model

prediction of the line intensity ratios used for the n_e and T_e derivation.

Acknowledgments

The authors would like to thank Prof. J.D. Hey for providing calculations of Zeeman splitting and perturbed line strengths as well as for comments on the manuscript, Dr. G. Sergienko for very helpful suggestions, Dr. J. Geiger and Dr. A. Werner for discussions and Mr. Klaus Klören for technical assistance.

[1] B. Schweer, G. Mank, A. Pospieszczyk, B. Brosda, and B. Pohlmeyer. Electron temperature and electron density profiles measured with a thermal He-beam in the plasma boundary of TEXTOR. *J. of Nucl. Mater.*, 196-198:174–178, 1992.

[2] M. Brix. *Messung von Elektronentemperatur und -dichte mittels Heliumstrahldiagnostik im Randschichtplasma eines Tokamaks*. Jülicher Report Jül-3638, 1998.

[3] U. Kruezi. *Entwicklung einer Heliumstrahldiagnostik zur Messung der Elektronendichte und -temperatur mit hoher räumlicher und zeitlicher Auflösung*, volume 62. Jülicher Report Jül-4220, 2007.

[4] A. Hidalgo, D. Tafalla, B. Brañas, and F.L. Tabarés. Multipulse supersonic helium beam diagnostic in the TJ-II stellarator. *Rev. Sci. Instr.*, 75:3478–3480, 2004.

[5] D. Andruczyk, S. Namba, B.W. James, K. Takiyama, and T. Oda. A short-pulsed compact supersonic helium beam source for plasma diagnostics. *Plasma Devices and Operations*, 14:81–89, 2006.

[6] T. Fujimoto. A Collisional-Radiative Model for Helium and its Application to a Discharge Plasma. *J. Quant. Spectrosc. Radiat. Transfer*, 21:439–455, 1979.

[7] B. Brosda. *Modellierung von Helium-Atomstrahlen und ihr Einsatz zur Plasmadiagnostik der Tokamakrandschicht*. Dissertation, Ruhr-Universität Bochum, 1993.

[8] P. Kornejew. *Bestimmung der Elektronenparameter in Randschichtplasmen unter Verwendung eines thermischen Heliumstrahls, IPP-8/10*. Max-Planck-Institut für Plasmaphysik, Garching, 1996.

[9] M. Goto and T. Fujimoto. *Collisional-radiative Model for Neutral Helium in Plasma: Excitation Cross Section and Singlet-Triplet Wavefunction Mixing*. Rep. NIFS-DATA-43, NIFS, Nagoya, 1997.

[10] M. Brix and B. Schweer. . *Proc. 24th EPS Conf. on Controlled Fusion and Plasma Physics (Berchtesgarden)*, 21A:1837–1840, 1997.

[11] H.P. Summers and M.G. O'Mullane. The Atomic Data and Analysis Structure. In R.E.H. Clark and D.H. Reiter (eds.), editors, *Nuclear Fusion Research. Understanding Plasma-Surface Interactions*. Springer-Verlag, Berlin, 2005.

[12] V.S. Burakov, N.V. Tarasenko, and N.A. Cheptsova. Lasers for plasma diagnostics and laser methods of investigation (review). *Journal of Applied Spectroscopy*, 54:321–333, 1991.

[13] K. Muraoka and M. Maeda. Application of laser-induced fluorescence to high-temperature plasmas. *Plasma Phys. Control. Fusion*, 35:633–656, 1993.

[14] R. F. Boivin. Laser induced fluorescence in Ar and He plasmas with a tunable diode laser. *Rev. Sci. Instrum.*, 74:4352–4360, 2003.

[15] Ph. Mertens and A. Pospieszczyk. Radial and spectral profiles of atomic deuterium in front of a limiter in TEXTOR-94: Results of laser-induced fluorescence at Lyman-α. *J. of Nucl. Mater.*, 266-269:884–889, 1999.

[16] F. Skiff and J.J. Curry. Nonlinear optical tagging and laser induced fluorescence. *Rev. Sci. Instrum.*, 66:629–631, 1995.

[17] U. Czarnetzki, D. Luggenhölscher, and H.F. Döbele. Space and time resolved electric field measurements in helium and hydrogen RF-discharges. *Plasma Sources Sci. Technol.*, 8:230–248, 1999.

[18] C. Honda and M. Maeda. Transient local magnetic field measurement in a bumpy torus by rapid-frequency-scan laser spectroscopy. *Rev. Sci. Instrum.*, 58:1593–1596, 1987.

[19] C.F. Burrell and H.-J. Kunze. Collisional transfer rates between excited levels in helium. *Phys. Rev. A*, 18:2081–2088, 1978.

[20] R. Denkelmann, S. Maurmann, T. Lokajczyk, P. Drepper, and H.-J. Kunze. Measurement of rate coefficients for electron-atom collisions in a helium plasma by laser-induced fluorescence. *J. Phys. B: At. Mol. Opt. Phys.*, 32:4635–4646, 1999.

[21] N.K. Podder, J.A. Johnson III, C.T. Raynor, S.D. Loch, C.P. Ballance, and S. Pindzola. Helium line intensity ratio in microwave-generated plasmas. *Physics of Plasmas*, 11:5436–5443, 2004.

[22] S. Kajita, N. Ohno, S. Takamura, and T. Nakano. Comparison of He I line intensity ratio method and electrostatic probe for electron density and temperature measurements in NAGDIS-II. *Physics of Plasmas*, 13:013301, 2006.

[23] A. Pospieszczyk, G. Chevalier, Y. Hirooka, R.W. Conn, R. Doerner, and L. Schmitz. Helium line emission measurements in PISCES-B as a tool for T_e-profile determinations in tokamak boundary plasmas. *Nuclear Instruments and Methods in Physics Research B*, 72:207–223, 1992.

[24] Y. Andrew and M.G. O'Mullane. Sensitivity of calculated neutral helium line intensities and their ratios to uncertainties in excitation rate coefficients. *Plasma Phys. Control. Fusion*, 42:301–307, 2000.

[25] U. Samm, P. Bogen, H. Hartwig, E. Hintz, K. Höthker, Y.T. Lie, A. Pospieszczyk, D. Rusbüldt, B. Schweer, and Y.J. Yu. Plasma Edge Physics in the TEXTOR Tokamak with Poloidal and Toroidal Limiters. *J. of Nucl. Mater.*, 162-164:24–37, 1989.

[26] O. Neubauer, G. Czymek, B. Giesen, P.W. Hüttemann, M. Sauer, W. Schalt, and J. Schruff. Design Features of the Tokamak TEXTOR. *Fus. Sci. Techn.*, 47:76–86, 2005.

[27] B. Schweer, S. Brezinsek, H.G. Esser, A. Huber, Ph. Mertens, S. Musso, V. Philipps, A. Pospieszczyk, U. Samm, G. Sergienko, and P. Wienhold. Limiter Lock Systems at TEXTOR: Flexible Tools for Plasma-Wall Investigation. *Fus. Sci. Techn.*, 47:138–145, 2005.

[28] E. Hintz and B. Schweer. Plasma Edge Diagnostics by Atomic Beam Supported Emission Spectroscopy - Status and Perspectives. *Plasma Phys. Control. Fusion*, 37:A87–A101, 1995.

[29] J.D. Hey, Y.T. Lie, D. Rusbüldt, and E. Hintz. Doppler Broadening and Magnetic Field Effects on Some Ion Impurity Spectra Emitted in the Boundary Layer of a Tokamak Plasma. *Contrib. Plasma Phys.*, 34:725–747, 1994.

[30] J.D. Hey, C.C. Chu, and Ph. Mertens. Zeeman spectroscopy of tokamak edge plasmas. *'Spectral Line Shapes', Proceedings of the 16th International Conference on Spectral Line Shapes (Berkeley 2002), AIP Conference Proceedings No. 645*, 12:26–39, 2002.

[31] P. Bogen, H. Hartwig, E. Hintz, K. Höthker, Y.T. Lie, A. Pospieszczyk, U. Samm, and W. Bieger. Properties of the TEXTOR boundary layer. *J. Nucl. Mater.*, 128-129:157–162, 1984.

[32] A. Pospieszczyk and G.G. Ross. Use of laser-ablated fast particle beams for the measurement of n_e and T_e profiles in the TEXTOR boundary layer. *Rev. Sci. Instr.*, 59:1491–1493, 1988.

[33] W. Lochte-Holtgreven. Evaluation of Plasma Parameters. In W. Lochte-Holtgreven, editor, *Plasma Diagnostics*. North-Holland Publishing Company, Amsterdam, 1968.

[34] K. Takiyama, H. Sakai, M. Yamasaki, and T. Oda. Measurement of Density Distribution of Metastable He Atom in a Plane-Parallel Hollow Cathode He Plasma. *Jpn. J. Appl. Phys.*, 33:5038–5045, 1994.

[35] K. Takiyama, T. Katsuta, M. Watanabe, S. Li, and T. Oda. Spectroscopic method to directly measure electric field distribution in tokamak plasma edge. *Rev. Sci. Instrum.*, 68:1028–1031, 1997.

[36] J.D. Hey, M. Korten, Y.T. Lie, A. Pospieszczyk, D. Rusbüldt, B. Schweer, B. Unterberg, J. Wienbeck, and E. Hintz. Doppler Broadening and Magnetic Field Effects on the Balmer Lines Emitted at the Edge of a Tokamak Plasma. *Contrib. Plasma Phys.*, 36:583–604, 1996.

[37] O. Schmitz. *Experimentelle Untersuchung der Plasmastruktur und Charakterisierung des Transportverhaltens in der laminaren Zone einer stochastisierten Plasmarandschicht*. Jülicher Report Jül-4220, 2006.

[38] M. Krychowiak, Ph. Mertens, B. Schweer, S. Brezinsek, R. König, O. Schmitz, M. Brix, T. Klinger, and U. Samm. LIF Measurements on an Atomic Helium Beam in the Edge of a Fusion Plasma. *Proc. 34th EPS Conf. on Plasma Physics (Warsaw)*, pages P–2.142, 2007.

[39] A. Hidalgo, F.L. Tabarés, and D. Tafalla. Testing of the collisional-radiative model by laser-induced perturbation of a supersonic He beam in TJ-II plasmas. *Plasma Phys. Control. Fusion*, 48:527–536, 2006.

[40] K. Tsuchida, S. Miyake, K. Kadota, and J. Fujita. Plasma electron density measurements by the laser- and collision-induced fluorescence method. *Plasma Physics*, 25:991–999, 1983.

[41] D.A. Shcheglov, S.I. Vetrov, I.V. Moskalenko, A.A. Skovoroda, and D.A. Shuvaev. Laser Spectroscopy for Measuring the Parameters of a Plasma Containing Helium and Argon. *Plasma Physics Reports*, 32:119–122, 2006.

[42] P. Chall, E.K. Souw, and J. Uhlenbusch. Laser diagnostics of a low-pressure hollow-cathode arc. *J. Quant. Spectrosc. Radiat. Transfer*, 34:309–320, 1985.